The Influence of Heat Input Ratio on Electrical Power Output of a Dual-Core Travelling-Wave Thermoacoustic Engine

Wigdan Kisha[1*], Paul H. Riley[2], Jon McKechinie[3], David Hann[4]

[1, 3,4] Faculty of Engineering, University of Nottingham, UK

[2] School of Mathematics, Computer Science & Engineering. City, University of London, UK

Corresponding author: *Email address: wigdan.kisha@nottingham.ac.uk

Abstract

This paper presents an analytical and experimental investigation of an electricity generator that employs a two-stage looped tube travelling-wave thermoacoustic prime-mover to deliver acoustic power from heat energy, a loudspeaker to extract electricity from sound energy and a tuning stub to compensate the changes in the acoustic field within the engine to enable close to travelling wave operation at the loudspeaker. Furthermore, the paper explains how to enhance the output power utilizing different heat input ratios through the engine cores. A well-known thermoacoustic design tool called DeltaEC is used to simulate the wave propagation through the different parts of the system. The electrical power predicted from the low-cost prototype was 24.4 W acoustic power which confirms the potential for developing low-cost thermoacoustic electricity generator for heat recovery from low-grade heat sources. The electrical power can be increased to 31.3 W using different heating power percentages through the two units. The verified experimental data shows good agreement with DeltaEC results.

Keywords: Regenerator, thermoacoustic, acoustic power, loudspeaker as a generator, DeltaEC

Background

The development of new techniques utilizing low-temperature waste heat and renewable energy sources have drawn enormous attention worldwide in recent years. There are many sources of such low-grade heat that, if they could efficiently and economically be harvested, would decrease carbon footprint significantly. One application where it has the potential to make significant changes to the standard of life is in the generation of electricity in low-income rural areas of the world. Over three billion people in the developing world use open fires for cooking process and one billion do not have access to electricity. An estimated 4 million people die prematurely by the smoke from open fires, mostly women, and children, making this one of the serious health threats facing people in developing countries [1]. The target of this research is to provide healthy cooking and electric power for the households of Sudan and South - Sudan countries by means of thermoacoustic technology.

Thermoacoustics is a new promising technique that uses heat to produce high-intensity sound waves which can, in turn, produce electricity. A thermoacoustic engine (TAE) eliminates the majority of mechanical moving parts by its simple construction, which comprises an acoustic resonating tube and a section of porous media in between two heat exchangers [2]. The well-known torus configuration travelling-wave engine developed by Backhaus and Swift has demonstrated a high efficiency of 30% which corresponds to 41% Carnot efficiency using 30 bar pressurized helium at a high operating temperature of 725˚C [3], which is comparable to the efficiencies from petrol and diesel engines, but at lower temperatures, although efficiency is much lower when a flame is used as heat [4]. At these high temperatures travelling wave thermoacoustic engine has to compete with other conventional devices such as Stirling engine. However, clearance sealing is an issue in conventional Stirling engine at high temperature.

Several variations of systems have been attempted to convert the acoustic power to useful electric power, utilizing different system configurations and transduction mechanisms [5, 6]. Thermoacoustic stoves have been shown to be a cheap option compared to others in situations where hydropower is not available, but since the technology is relatively new, and these low temperature systems are subject to non-linear affects that are not well understood, present work is concentrating on understanding the non-linear effects and minimising the losses.

The idea of thermoacoustic power has been proved over the last 20 years since the first working engines were produced. A number of designs have been developed that can achieve good efficiencies relative to Carnot for. An early thermoacoustic engine was designed for space application using a flexure-bearing linear alternator, the electrical power produced from this engine was 39 W with 18% thermal-to-electrical efficiency [7, 8]. A novel three-cylinder double-acting thermoacoustic Stirling electricity generator was developed and tested [9], using 3.12 KW heating power from each heater block and three alternators to extract the electric power. 5 MPa pressurized helium was adopted as the working gas and the system produced a maximum electrical power of 1570 W. The performance was highly degraded due to the significant difference in the performance of the engines and the alternators. Another investigation on generating electricity using multiple- stage travelling-wave thermoacoustic engines was undertaken by Kang et al.[10]. In this case, the total electric power output had a maximum value of 204 W using 1.8 MPa helium and 6 kW total heating power (with the same input through the two heaters). The parasitic heat loss in the experiments was very large and there was non-linear behavior in the system due to the high-pressure amplitude. Most recently, a three-stage travelling-wave thermoacoustic electricity generator was proposed by Bi et al. [11]. This prototype achieved a maximum electric power of 4.69 kW with thermal-to-electric efficiency of 15.6% using 6 MPa helium gas. The heat transfer was again poor and there were large flow losses and friction losses from the alternator which dropped the power rate.

The conversion of the acoustic field to electrical output is mostly carried out using linear alternators, although more recently bi-directional turbines have shown some potential in improving performance [12]. Linear alternators purpose-designed for thermoacoustic systems are expensive, which limit the advantages of the thermoacoustic heat engines for low-cost energy conversion applications and therefore, it is possible to consider low-cost commercial available loudspeakers to convert acoustic power gain into electricity. In these low cost applications the main driver is the cost of the system, not the transduction efficiency [13, 14]. In 2012, SCORE project (www.score.uk.com) developed and tested two low-cost double-regenerator traveling-wave thermoacoustic electricity generators, to produce electricity using waste heat energy from cooking stoves. A propane-driven stove delivered approximately 15 W of electricity. While, a wood burning cooking stove was successfully demonstrated 22.7 W of electricity. The performance of the devices was low due to the high acoustic losses and the inefficient linear alternators being used [15], but also because, at these low temperatures, the system is very sensitive to losses. Understanding this and minimising losses is important if we want to reach the commercially needed target of producing at least 100 W of electrical power from a cook-stove that costs less than £200.

Many of the configurations that have been tested use multiple stages and it has been the practice to input the same amount of heat in each exchanger. In this paper, a new operational methodology using different percentages of thermal energy is employed for the optimization of the system for the first time. This paper will look at whether there is a strategic advantage in varying the heat power ratio.

Modeling of the system

To further understand the behavior of the thermoacoustic system considered in this research and to predict the performance of the existing build engine, a design software code referred as

DeltaEC (Design Environment for Low-amplitude ThermoAcoustic Energy Conversion) is utilized [16]. DeltaEC integrates numerically the wave equation and other equations such as the energy equation throughout the whole system in one spatial dimension based on a low-amplitude "acoustic" approximation and sinusoidal time dependence of the variables [17]. The governing equations used in DeltaEC as follows:

$$\frac{dp_1}{dx} = -\frac{i\omega\rho_m}{A_g(1-f_v)}U_1 \quad (1)$$

$$\frac{dU_1}{dx} = -\frac{i\omega A_g}{\gamma P_m}(1+(\gamma-1)f_k)p_1 + \frac{(f_k-f_v)}{(1-f_v)(1-\sigma)}\frac{1}{T_m}\frac{dT_m}{dx}U_1 \quad (2)$$

Where: p_1 pressure amplitude of oscillation (Pa), U_1 volumetric velocity amplitude (m^3/sec), ω angular velocity which equals $2\pi f$ (rad/sec), ρ_m mean density (kg/m^3), P_m mean pressure of the working gas (Pa), T_m mean temperature of the working gas (K), γ is the ratio of the specific heats of the gas, f_k is the thermal spatially averaged diffusion function, f_v is the viscous spatially averaged diffusion function, σ is Prandtl number, A_g is the cross-sectional area available for the gas, A_s is the cross-sectional area of the solid. This model was validated against experimental results shown below to confirm the findings.

Explanation of test-bed apparatus

The SCORE system comprises a two-stage thermoacoustic engine operating in mainly travelling wave mode, with two tuning stubs and a loudspeaker as shown in Figure 1. Which is based on the loop-tube configuration. This arrangement gives an advantage of using low-temperature heat source with a lower temperature gradient through each stage [18, 19]. Both stages comprise an ambient heat exchanger (AHX), regenerator, hot heat exchanger (HHX), thermal buffer tube (TBT) and a secondary ambient heat exchanger (SAHX) as in Figure 1(b). The AHX is made out of the core of a commercial low-cost car radiator, suitably modified to fit the thermoacoustic engine. A thermos-siphon water circulation method was applied to take heat from the system, so a pump isn't required in the system. To maintain a low cost for the engine core and to achieve a quick warm-up time, a low-mass convoluted stainless steel plate design has been adopted for the HHX. The HHX is $233 \times 307\ mm$ and is made out of 3 mm thick Stainless steel plate. The plate was welded to a flange that designed to be directly bolted to the engine housing. The regenerator is sandwiched between the AHX and the HHX and was formed by stacking 50 pieces, 80-mesh Stainless-steel wire mesh machined to a required size of $20 \times 20\ mm$. The mesh wire has a diameter of $95\ \mu m$ and a pitch of $250\ \mu m$. The AHX and the HHX are clamped between upper and lower housings [5]. The TBT is simply a section of stainless steel pipe and is located below the HHX to separate the SAHX from the hot gas and thus minimizing parasitic heat losses. A SAHX is introduced after the TBT to cool the air before it flows to the alternator. The stages are connected using 70 mm diameter standard PVC pipes and fittings. Two extra pipes perpendicular to the feedback loop "denoted as tuning stubs" are introduced in the loop to enhance the impedance matching between the acoustic wave and the linear alternator and to maintain the phase angle between the velocity and the pressure in a travelling-wave condition through the regenerators. To extract the electric power from the circulating acoustic power, a low-cost commercial loudspeaker (model JL 6W3v3-4) was used as a linear alternator and is connected in series in the loop. This arrangement allows suppressing the acoustic streaming which could cause heat dissipations from a HHX. To simulate more closely to the final application, two custom-made electrical heaters are used to supply the heat to the HHXs. For temperature measurements, eight thermocouples (Type-K) were placed in different locations to monitor the hot and the cold temperatures of each regenerator unit as well as the

temperatures the cooling water. Three absolute pressure transducers (model IMPRESS) were distributed along the feedback pipe and a differential pressure sensor (model ABPMJJT015PGAA5) was used to capture the volumetric flow rate across the loop. The readings of the thermocouples and the pressure transducers were collected by a Data Acquisition system (NI cDAQ 9172) which is connected to a data logger system. To harvest the electrical power from the system, a wide range variable resistor (model VISHAY®) was adjusted to the optimal electrical load for the loudspeaker. The voltage and the current from the alternator are measured using a power analyzer (model KintiQPPA2530).

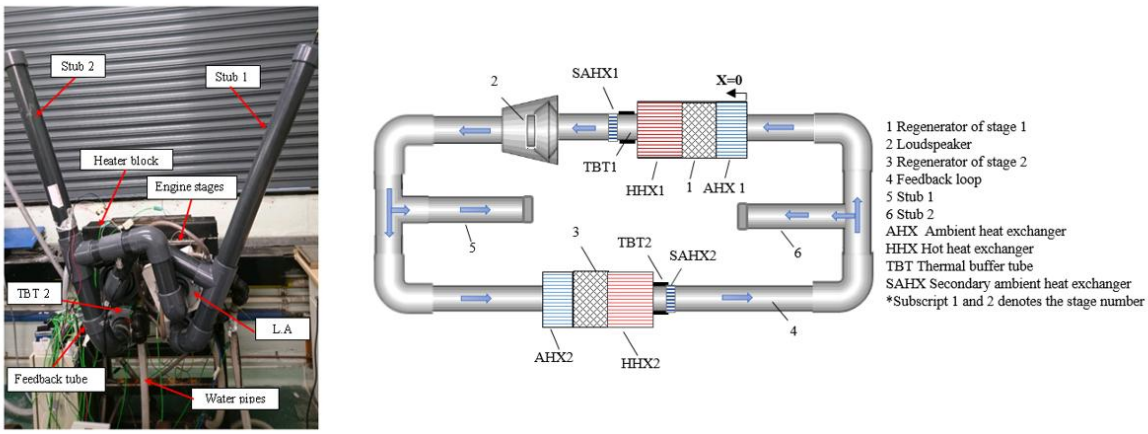

Figure 29. The two-stage thermoacoustic electricity generator. (a) Photo of the system. (b) Functional diagram

In order to address the performance of the system, it is important to estimate the flow of the acoustic power which is defined as a time-average energy flux accompanied by pressure oscillations and velocity of the working gas. The most common method to measure the acoustic power is the so-called two-microphone method [20]. Conceptually, this method employs two absolute pressure sensors to obtain the velocity of the oscillating gas. However, one of the drawbacks of this technique is obtaining the high accuracy of the phase angle between the pressure and the velocity. Therefore, to get a more durable way of measuring the acoustic power, an alternative method referred as "gradient method" is used in the current system. It employs one absolute pressure transducer and one differential pressure sensor to directly calculate the mass of the air between the two sensors, the acoustic velocity, and the acceleration. The distance between the two sensors is small compared to the two-microphone method. Therefore, no empirical correction for acoustic loss is required. The acoustic power propagation in the feedback loop can be given as [21]:

$$P_{Ac.} = \mathrm{A}.\hat{p}_1 \frac{\Delta \mathrm{p}_1}{2\omega\rho_m \Delta x} \sin \emptyset \qquad (3)$$

Here: A is the cross-sectional area of the feedback loop, p_1 is the pressure amplitude (Pa) which is the signal from the absolute sensor, Δp_a is the output signal of the differential pressure sensor (Pa), Δx is the distance between the two probes of the differential sensor (m), $\emptyset$ is the measured phase between p_1 and Δp_1, ω is the angular velocity (rad/sec), ρ_m is the mean density (kg/m³), p_m is the mean pressure (Pa).

Since the application is for the developing world, air at atmospheric pressure is used as the working gas. The maximum hot and the cold temperatures were set to 650 ºC and 90 ºC, respectively and the total heat input power was varied between 2.1 - 3 kW. This was split at different ratios between the two stages. DeltaEC model had predicted that changing the heat ratio to each core could affect the performance, so in the experiment the heat was inputted as

40%-60%, 50%-50%, 55%-45%, 60%-40%. The system operates at working frequency of 73 Hz. To verify the numerical results with the lab data, the load resistance of the loudspeaker was adjusted to 35.5 Ohm. In most applications the heat input would be split between the two cores evenly, providing Q/2 W to each core. In this paper we have investigated whether the results of the model which suggested that a 60% - 40% split would improve performance. These results are used to validate the numerical model.

Results and discussion

The schematic diagram of the model used in DeltaEC simulation is presented in Figure 1 (b)The model was constructed using the same design parameters of the existing prototype and using some of DeltaEC segments [17]. The model starts at x = 0 which is located at the hot end of the first AHX and goes anticlockwise until it returns. The pressure amplitude, the volumetric velocity amplitude, and their phases are adjusted so that they match at the start and the end of the model. The acoustic power flow is indicated by the blue arrows. Figure 2 demonstrates how the key acoustic parameters obtained from DeltaEC vary around the system. The 4 curves correspond to varying heat input into the two cores, with 40%, 50 % 55% and 60% of the heat being directed to core 1, which is just before the linear alternator, and the power in core 2 being adjusted to that the total energy input was a constant. No other variables were adjusted. It is clear that the curves have the same trend among the four heat supply percentage. In Figure 2(a), the Pressure amplitude drops at each of the two regenerators due to their flow resistance. It also decreases across the linear alternator due to its acoustic resistance. The two stubs don't influence the pressure amplitude. The standing wave ratio in the system is approximately around 2.97 due to the reflections where the feedback pipe area changes.

These numerical results demonstrate that using 60% of the heat in the first HHX resulted in higher pressure drop across the alternator diaphragm which indicates better extraction of the electric power. In other words, the electrical power output increased from X to Y when the balance of heat went from 50% to 60%, an X% increase. It can be seen that the pressure anti-nodes altered location slightly in the four heat supply ratios, particularly near the end of the feedback loop due to the slight change in the operating frequency. There is a high decrease in the flow at the location of the stub which indicates that the stub removes part of the volumetric flow from the loop. In contrast, the volumetric velocity increases significantly along the two regenerators due to the sharp temperature gradient across them. Between the alternator and the SAHX, there is a part of connecting pipe where the volumetric velocity increases due to the change in the area. The acoustic impedance Figure 2(c) has high values at the cold end of the two regenerators which led to $[|Z| * A/a * \rho_m] \sim 7$ & 12 at regenerator 1 and regenerator 2, respectively. In travelling-wave thermoacoustic engines, a common practise is to set the absolute value of the regenerator impedance in the range of 10-20 time the gas characteristic impedance [19]. At the locations of the tuning stubs, the impedance decreased due to the constant pressure amplitude at the junction between the stub and the feedback tube. The acoustic loop power Figure 2(d) increases when adding higher heat in the first HHX. Again for all the cases, the curve has the same characteristics, but it is clear that there is higher acoustic power when the ratio of heat input is 60% / 40%. Considering the case where the total heat splits eventually between the two heaters, the results revealed that, around 58.4 W of the acoustic power from the resonance tube is introduced into unit 1 and only about 1 W is dissipated within its AHX, leading to an amplification of 57.4W. This is then fed into the cold side of the regenerator where the acoustic power is amplified to 77.5 W. Minor acoustic loss of 1.8 W occurred through the HHX, the TBT and the SAHX of the first unit. The alternator delivered 24.4 W electrical power with a thermal-to-acoustic efficiency of 2.3%, and thermal-to-electrical efficiency of 0.98%.

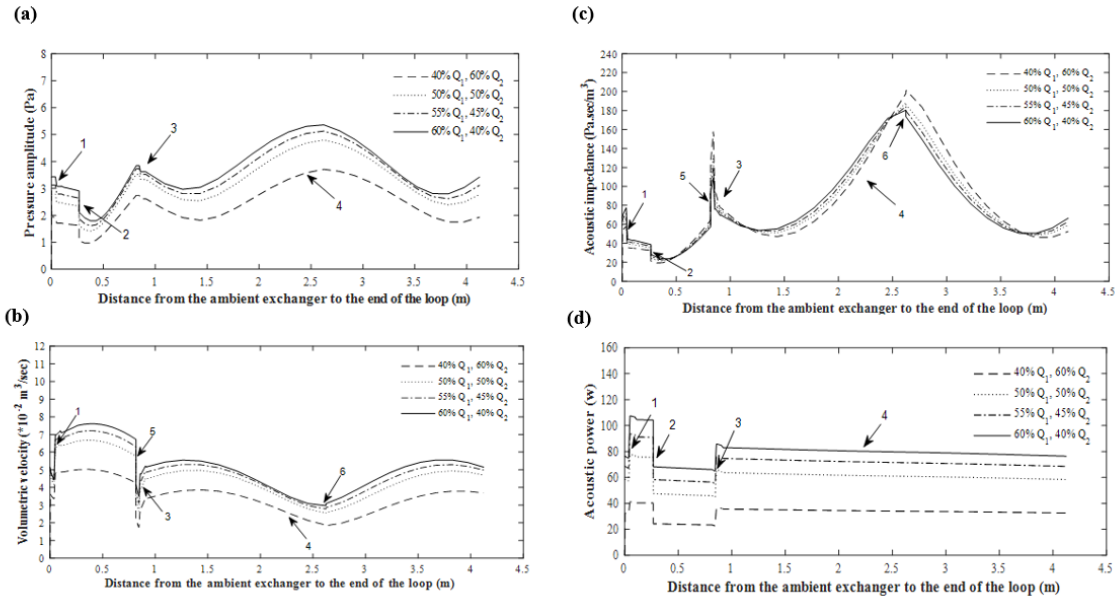

Figure 2. The variation of the key performance parameters through the loop using different percentages of the total heat input: $\boldsymbol{Q_1}$ in heater 1 and $\boldsymbol{Q_2}$ in heater 2 (a) Pressure amplitude (b) volumetric velocity (c) acoustic impedance (d) acoustic power. * Numbers from 1 to 6 correspond to the defined ones in Figure 1

The results of the numerical modelling were surprising, thus the performance of the experimental rig was assessed using the same concept. Figure 3 compares the lab results of several percentage of the heat power (range 2.1 to 3 kW). Both the acoustic power and the electric output increase linearly with the total heat input. Extra power could be gained by simply supplying a higher heat percentage to the first HHX. This can be justified by the location of the loudspeaker which is immediately after the TBT of the first engine. Using 2.5 kW power with 50% Q_1 , 50% Q_2 generated 48.4W acoustic power. This power is raised to 68 W when using 60 % Q_1 , 40% Q_2 which resulted in an extra 6.5 W electric power (10% increase). However, DeltaEC models predict loop power as high as 0.1- 2.8 percent, and electric power as high as 0.4 to 3.7 percent which indicates that the system isn't quite efficient in converting heat energy into acoustic power and the heat dissipation is potentially an issue. The alternator in this system is installed next to the SAHX of the first unit. At this location, the acoustic impedance has a low value. In fact, almost a maximum alternator stroke is reached at 3 kW thermal power. Therefore, if more electrical power is to be extracted, the alternator should be placed in a high-impedance zone to avoid the stroke limitation.

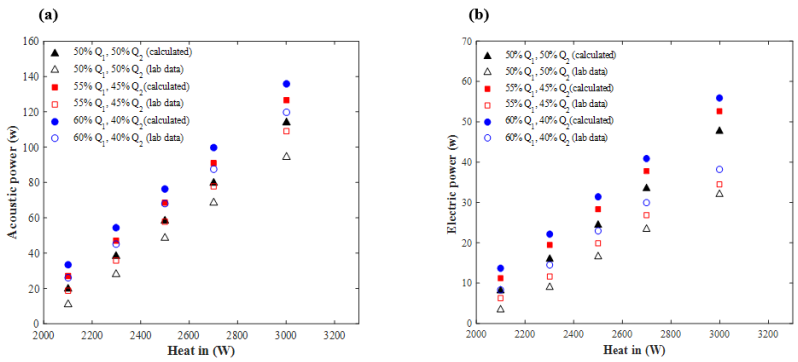

Figure 3. Performance of the engine under four heat input ratios. (a) Acoustic power (b) Electrical power

The thermal-to-electric efficiency reached a maximum value of 1.25% when using 60 % Q_2, which is indeed much lower than that noted in Ref [8], where the linear alternator acted as a

mechanical resonator as well as a transduction mechanism. In the current design, two reasons are contributed to the poor efficiency. The first one, using a linear alternator instead of resonating tube minimizes the acoustic losses where the long resonator dissipated a considerable amount of the loop power. The second reason, the transduction efficiency of the loudspeaker is quite low (about 34%) compared to the linear alternator which was approximately around 90%. However, the linear alternator is expensive and this counteracts the affordability of the system. Therefore, the loudspeaker is a viable competitive candidate for developing a thermoacoustic generator.

The onset temperature is also important. Low onset temperatures can help improve efficiency. Therefore, the electric power against the temperature difference across the two regenerators is plotted in Figure 4 for several heat input percentages. Clearly, the amplification in the second core decreases when the heat input into the core decreases and the onset temperature increases. However, in the first core, the reverse happens. In fact, the onset temperature of the first core drops significantly and by much more than the increase in the second core. Reversing the heat ratio results in reduced performance. Further study is required to find out why this occurred. The onset temperature difference and the steepness of the power against temperature curve are indicators of the performance of a thermoacoustic system. A low onset temperature means low loss and adequate acoustic matching between the various components of the system. A steep temperature curve reflects good heat transfer of the ambient and the hot heat exchangers and also indicates low acoustic dissipation [19]

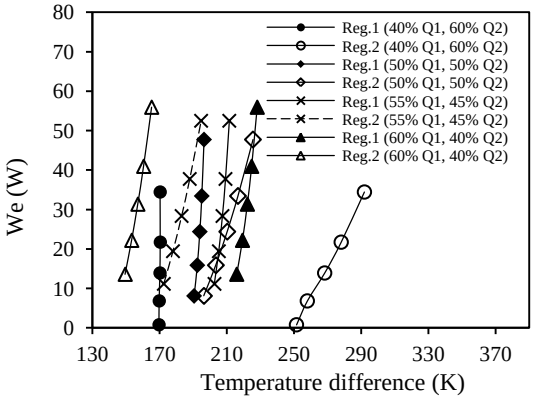

Figure 4. Electric power relation with the temperature difference across the regenerator

Summary

In this paper, the influence of the heat input ratio into a looped-tube thermoacoustic engine was discussed. The engine converts acoustic power to electrical energy using a commercially available low-cost loudspeaker. DeltaEC is used to simulate the acoustic field within the system. DeltaEC results reflect that the electrical power output from the system equals 24.4 W from 2.5 kW heat input. An extra 7 W of electricity could be obtained by applying 60% of the heat into the first hot heat exchanger. DeltaEC models predict acoustic loop power as high as 0.1- 2.8 percent, and electric power as high as 0.4 to 3.7 from the lab data percent which indicates that the system isn't quite efficient in converting heat energy into acoustic power and the thermal dissipation is potentially an issue.

References:

[1] A. A. Cruz, *Global surveillance, prevention and control of chronic respiratory diseases: a comprehensive approach*: World Health Organization, 2007.

[2] S. Backhaus and G. W. Swift, "A thermoacoustic-Stirling heat engine: Detailed study," *The Journal of the Acoustical Society of America*, vol. 107, pp. 3148-3166, 2000.

[3] S. Backhaus and G. W. Swift, "A thermoacoustic Stirling heat engine," *Nature,* vol. 399, pp. 335-338, May 27 1999.
[4] P. H. Riley, "The myth of the high-efficiency external-combustion Stirling engine," *Engineering,* vol. 7, pp. 789-795, 2015.
[5] B. Chen, A. A. Yousif, P. H. Riley, and D. B. Hann, "Development and Assessment of Thermoacoustic Generators Operating by Waste Heat from Cooking Stove," *Engineering,* vol. Vol.04No.12, p. 4, 2012.
[6] Z. Yu and A. J. Jaworski, "Demonstrator of a combustion driven thermoacoustic electricity generator for remote and rural areas of developing countries," in *19th International Congress on Sound and Vibration 2012, ICSV 2012*, Vilnius, 2012, pp. 1581-1588.
[7] M. Petach, E. Tward, and S. Backhaus, "Design and testing of a thermal to electric power converter based on thermoacoustic technology," in *2nd International energy conversion engineering conference. The American Institute of Aeronautics and Astronautics, Providence, Rhode Island*, 2004.
[8] S. Backhaus, E. Tward, and M. Petach, "Traveling-wave thermoacoustic electric generator," *Applied Physics Letters,* vol. 85, pp. 1085-1087, 2004.
[9] Z. Wu, G. Yu, L. Zhang, W. Dai, and E. Luo, "Development of a 3 kW double-acting thermoacoustic Stirling electric generator," *Applied Energy,* vol. 136, pp. 866-872, 2014.
[10] H. Kang, P. Cheng, Z. Yu, and H. Zheng, "A two-stage traveling-wave thermoacoustic electric generator with loudspeakers as alternators," *Applied Energy*, vol. 137, pp. 9-17, 2015.
[11] T. Bi, Z. Wu, L. Zhang, G. Yu, E. Luo, and W. Dai, "Development of a 5 kW traveling-wave thermoacoustic electric generator," *Applied Energy,* vol. 185, pp. 1355-1361, 2017.
[12] K. De Blok, P. Owczarek, and M. François, "Bi-directional turbines for converting acoustic wave power into electricity," in *Proceedings of 9th PAMIR International Conference on Fundamental and Applied MHD*, 2014.
[13] P. H. Riley, C. Saha, and C. Johnson, "Designing a low-cost, electricity-generating cooking stove," *IEEE Technology and Society Magazine*, vol. 29, pp. 47-53, 2010.
[14] C. R. Saha, P. H. Riley, J. Paul, Z. Yu, A. J. Jaworski, and C. M. Johnson, "Halbach array linear alternator for thermo-acoustic engine," *Sensors and Actuators, A: Physical*, vol. 178, pp. 179-187, 2012.
[15] B. Chen, P. Riley, Y. Abakr, K. Pullen, D. Hann, and C. Johnson, "Design and development of a low-cost, electricity-generating cooking Score-Stove™," *Proceedings of the Institution of Mechanical Engineers, Part A: Journal of Power and Energy,* vol. 227, pp. 803-813, November 1, 2013 2013.
[16] G. W. Swift and S. L. Garrett, "Thermoacoustics: A Unifying Perspective for Some Engines and Refrigerators," *The Journal of the Acoustical Society of America,* vol. 113, pp. 2379-2381, 2003.
[17] W. C. Ward and G. W. Swift, "Design environment for low-amplitude thermoacoustic engines," *The Journal of the Acoustical Society of America*, vol. 95, pp. 3671-3672, 1994.
[18] K. de Blok, "Novel 4-stage traveling wave thermoacoustic power generator," in *ASME 2010 3rd joint US-European fluids engineering summer meeting collocated with 8th international conference on nanochannels, microchannels, and minichannels*, 2010, pp. 73-79.
[19] K. D. Blok, "Low operating temperature integral thermo acoustic devices for solar cooling and waste heat recovery," *The Journal of the Acoustical Society of America,* vol. 123, pp. 3541-3541, 2008.
[20] A. M. Fusco, W. C. Ward, and G. W. Swift, "Two-sensor power measurements in lossy ducts," *The Journal of the Acoustical Society of America*, vol. 91, pp. 2229-2235, 1992.
[21] K. de Blok, "Acoustic power measurements in thermoacoustic systems," Aster Thermoacoustics, 2013.

Experimental and Numerical Study of the Thermal Performance of Water-Stainless Steel Heat Pipes Operating in Mid- Level Temperature

Silva. Débora de O.[1], Riehl. Roger R.[2*]

[1]PhD Student, Space Mechanics and Control Division - DMC

[2]Senior Research Engineer and Faculty, Space Mechanics and Control Division – DMC

National Institute for Space Research, São José dos Campos, 12227-010 SP Brazil,

[*]E-mail: roger.riehl@inpe.br

Abstract

Thermal performance of water-stainless steel screen mesh wick heat pipes was investigated in this study. Three screen mesh wick heat pipes were fabricated and tested all different inclinations, and their thermal conductance in different modes were compared (experimental, calculated and numerical). The different mesh numbers can bring different meanings in terms of both liquid flow resistance and capillary pumping. The aim was to analyze the thermal behavior in the permanent and transient regime for each power when operated with the power step in mid-level temperature, for use in several industrial and aerospace applications when those levels of temperature are required. The calculated thermal conductances based on the thermal resistance analysis were used to be compared with the obtained experimental thermal conductances. An adjustment factor was calculated with the objective of being used in the results of the calculated thermal conductances to bring them closer to the actual results that were obtained experimentally with the water-stainless heat pipes. The numerical approaches undertaken in analysing the transient thermal performance was used the multifluid model where two different fluid zone were created to represent vapour flow in the middle and liquid flow in the porous wick. The predicted surface temperatures with varying heat inputs (25 W - 125 W) from the numerical model and experimental tests were used for thermal conductance (numerical and experimental) were compared with calculated thermal conductance.

Keywords: heat pipe, experimental heat pipe, simulation, thermal performance.

Introduction

Heat pipes are passive heat transfer devices that can successfully transfer large amounts of heat. The robust and simple tubular structure with no moving parts makes the heat pipe a perfect choice for different applications such as industrial or aerospace. The application of heat pipes have increased over the last 20 years and can be seen in many areas such as industrial and aerospace, due to their high capacity of heat transport. Heat Pipes have been successfully applied for space missions where the operational conditional are extremely severe; ground applications have found then to be very important devices to be considered for the heat dissipation issues faced by new projects [1-4]. Applications vary from satellites and spacecrafts to computer's cooling, but heat pipes have gained attention for other applications as well, especially those related to military and surveillance systems [4]. The continuous development of the heat pipe technology has given to this passive thermal control device a great interest for the new applications that were not considered before. Special attention should be given to heat pipes that operate at mid-level temperatures (up to 200° C), which have found several applications in both aerospace and industrial areas [4]. The thermal transient behaviour of the heat pipe is an important aspect in the evaluation of the heat pipe performance, particularly during the start-up period. The transient analysis would indicate whether the start-up is too fast, which could lead to evaporator section being overheated and consequently reducing the heat pipe efficiency. A number of experimental studies on the transient behaviour of heat pipes have been investigated, which further validated by numerical simulation [5]. Kempers et al. [6] realized an experimental study to determine the effect of the number of mesh layers and amount of working fluid on the heat transfer performance of water-copper heat pipes with screen mesh wicks. For the heat pipes with the smaller number of

mesh layers, the effective thermal resistance was non-linear, especially at low heat flux and the thermal resistance decreases significantly with the heat flux, and then approaches a constant value. In the nearly constant region, the thermal resistance increases with the number of mesh layers. However, a six fold increase in the number of mesh layers resulted in only a 40% increase in thermal resistance of the heat pipe [6]. Kempers et al. [7] investigated experimentally the heat transfer mechanisms in the condenser and evaporator section of a water-copper wicked heat pipe. The heat transfer was characterized by measuring the internal and wall temperature distributions under different operating conditions and as the heat transfer is dependent on the vapour pressure and heat flux, with boiling occurring even for very low heat fluxes, or superheat for operating temperatures above 50°C the onset of boiling in the evaporator could be reasonably predicted using a bubble nucleation criterion. Silva and Riehl [8] conducted an experimental investigation for copper-water heat pipes with different mesh number for heat pipes operating in different inclinations. In the series of tests, the heat input to the evaporator was increased in steps of 25 W until 125 W and presented start-ups without oscillations of temperatures, reaching the temperature of the evaporator, adiabatic and condenser near the isothermal condition. Therefore, the heat pipes confirmed good performances when analysed by their thermal conductances [9] and compared with experimental results between copper and stainless steel heat pipes. In this paper, heat pipes were designed and manufactured with the objective of investigating the potential application of heat pipes operating at mid-level temperature. The thermal conductance obtained from the experimental tests were used to correlate the thermal conductances obtained analytically, with results showing high accuracy based on the adjustment factor applied. A numerical model was made for analyzing the transient thermal performance of heat pipes with screen mesh wick and the results validated with the experimental results.

Experimental Investigation

In order to investigate the potential application of heat pipes for industrial use, were designed and manufactured three heat pipes for experimental tests shown in Figure 1. The heat pipes are stainless steel 316-L by its wide acceptance and application in industry and the compatibility with water. The geometrical properties of the heat pipe used in this experimental work is shown in Table 1. The heat was applied to the evaporator by a controlled electric heater, being used the testing power step, the heat source was applied to each heat pipe to observe, at first, the start-up effect. Once the temperatures for the start-up power have reached stability, power was changed according to the testing profile, following the sequence to temperature stabilization.

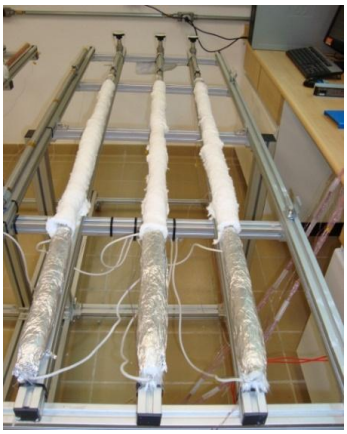

Figure 1 - Heat Pipes Experimental Bench.

The experimental test rig comprises a test bench, a DC power controller (Agilent N5749A), and a National Instrument SCXI data acquisition system controlled by LabVIEW. Six Omega T-type thermocouples with accuracy of ±0.3°C were used to measure the wall temperatures of each heat pipe in two locations of the evaporation, adiabatic and condenser sections. Another thermocouple was used for measuring the ambient temperature. All tests were performed under controlled room conditions, with the temperature set at 22°C ± 2°C. The condenser was open to the ambient air, exchanging heat by natural convection. Therefore, oscillations on the ambient temperature were expected due to the air conditioning on/off operation.

Table 1. Characteristics of heat pipes - HP1, HP2 and HP3.

Geometric Characteristics of the Experimental HP			
	HP 1	**HP 2**	**HP 3**
Evaporador/Adiabatic/Condenser/Total length (m)	0.25 / 0.9 / 0.35 / 1.5		
Working Fluid	Water		
Tube material	316L - SS		
Outside diameter (m)	0.01905		
Inside diameter (m)	0.0135		
Screen wick material	316L - SS		
Screen mesh number	100	200	400
N° of layers of wick	3		
Wick Porosity %	0.68	0.64	0.61
Wick Permeability (m^2)	$2.39x10^{-10}$	$5.16x10^{-11}$	$1.10x10^{-11}$
Mean pore radius (m)	$1.1827x10^{-4}$	$6.35x10^{-5}$	$3.18x10^{-5}$
Operating temperature range (° C)	22 - 160		
Operating Power (W)	25 - 125		

The heat source was a silicone flexible electric heater, being insulated by rock wool with the thermal conductivity of 0.04 W/m*K, which was wrapped around the adiabatic section to reduce the heat loss to the surroundings. Prior to charging the heat pipes, they were properly cleaned and evacuated at a vacuum level of 10^{-5} mbar. Charging was only performed once the heat pipe was able to sustain such a vacuum level for at least 12 h. At this point in the test procedure, it was made a pressurized verification test to determine if the fittings, enclosures, and/ or seams of the heat pipe cases were appropriately sealed. This was best done by pressurizing the case using conventional leak testing equipment to check the case for leaks.

The laboratory tests were conducted with the following procedures:

- The heat was applied to the evaporator by a controlled electric heater, being used the power of 25W, 50W, 75W, 100W and 125W per heat pipe;
- Heat was applied to each heat pipe to observe, at first, the start-up effect. Once the temperatures for the start-up power have reached stability (presenting variation of ±1°C during the last 20 minutes), the power was changed according to the testing profile, following the sequence to temperature stabilization. Once all power levels were tested, the power was switched off and waited for temperature equalization with ambient.

Thermal resistance analysis

The overall thermal resistance is comprised of nine different resistances arranged in series-parallel combination as shown by Fig. 2 [10,11]. In this model, the overall resistance of the cylindrical heat pipe is given by

$$R_T = R_{Pe} + R_{we} + R_v + R_{pc} + R_{wc} \quad (1)$$

The thermal resistance due to the pipe wall in the evaporator (R_{Pe}), liquid-wick at evaporator (R_{we}), liquid-wick at condenser (R_{wc}) and pipe wall in the condenser (R_{pc}) are

$$R_{pe} = \frac{\ln (d_0|d_i)}{2\pi L_e K_p}, R_{we} = \frac{\ln (d_i|d_v)}{2\pi L_e K_{eff}}, R_{wc} = \frac{\ln (d_i|d_v)}{2\pi L_c K_{eff}}, R_{pc} = \frac{\ln (d_0|d_i)}{2\pi L_c K_p} \quad (2)$$

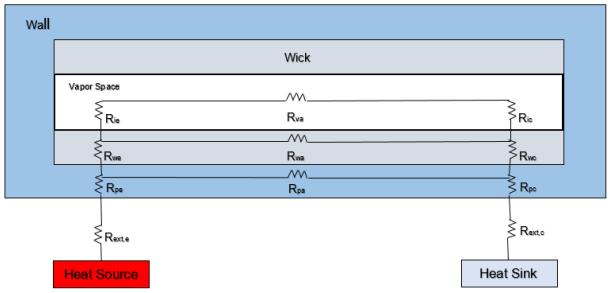

Figure 2. Overall thermal resistance of a heat pipe.

Where, the effective thermal conductivity of the wick structure is [10]

$$K_{eff} = \frac{k_l[(k_l+k_w)-(1-\epsilon)(k_l-k_w)]}{(k_l+k_w)(1-\epsilon)(k_l-k_w)} \quad (3)$$

The thermal resistance of the vapour flow, R_v is determined by [10]

$$R_v = \frac{\pi r_0^2 T_v F_v[(1/6)L_e+L_a+(1/6)L_e]}{\rho_v h_{f,g}} \quad (4)$$

Where F_v is the vapour frictional coefficient. Considering some simplifications, Chi [10] developed a simplified analytical equation to predict the approximate overall thermal resistance for a cylindrical heat pipe as follows

$$R_T = R_{Pe} + R_{we} + R_v + R_{pc} + R_{wc} \quad (5)$$

Summing all individual resistances (Eq. 5) and the comparative magnitudes of the resistance of the axial resistance of the pipe wall and liquid-wick combinations may be treated as open circuits and neglected. The theoretical thermal conductance of the heat pipe is then estimated as

$$G = \frac{1}{R_T} \quad (6)$$

The experimental results may raise possible variations, which came from heat pipe manufacturing standpoint and it affects heat pipe operation. Considering that the heat pipes were manually manufactured, an adjustment factor was taken into consideration for the thermal conductance results in such a way that it could result in a more accurate analysis in a way to put into consideration these possible variations. The adjustment factor is defined as follows

$$Factor = \frac{G_E}{G_{global}} \quad (7)$$

$$G_{global} = \alpha \frac{Q}{T_e - T_a} \quad (8)$$

where $0.8 \leq \alpha \leq 3.0$. The calculated thermal conductance used in this study for each power applied to the heat pipe can be defined as

$$G_C = \frac{1}{R_T} * Factor \quad (9)$$

With the consideration of the thermal conductance, it was expected that the calculated thermal conductance (theoretical with adjustment factor) presented the same trends of the ones obtained experimentally. The calculated thermal conductances, by the analysis of thermal resistances, do not consider important characteristics of an experiment, such as mounting characteristics for each heat pipe, volume of fluid inserted in each heat pipe, differences in the mesh of the porous structure after

inserted into each heat pipe, or even in the folding of the mesh for closing each heat pipe and etc. Therefore, adjustment factors for the thermal conductance calculated were considered for a better comparison with the results of the calculated and experimental thermal conductances.

Numerical Model

The working fluid is assumed to be liquid phase in the wick region (liquid zone) and vapour phase in the vapour region. When the evaporator is heated, the working fluid in the wick region is vaporized to the vapour space and the vapour flows to the condenser section. In the condenser section, after the vapour releases its latent heat to the environment through the outer surface of the condenser, it returns to the wick region as saturated liquid. For the mathematical formulation of this numerical unsteady simulation work, the following assumptions were made:

- Vapour and liquid flow are unsteady, 2-D, laminar and incompressible;
- Viscous dissipation and gravity effects are negligible;
- Heat generation or dissipation due to the phase change process in the heat pipe is ignored;
- The physical properties are constant;

With the above assumptions, the resulted governing equations in cartesian coordinates are as follows:

Vapour Flow Region

Continuity:

$$\frac{\partial u_v}{\partial x} + \frac{\partial v_v}{\partial y} = 0 \tag{10}$$

Momentum in the x-direction:

$$\rho_v \left(\frac{\partial u_v}{\partial t} + u_v \frac{\partial u_v}{\partial x} + v_v \frac{\partial v_v}{\partial y}\right) = \mu_v \left(\frac{\partial^2 u_v}{\partial x^2} + \frac{\partial^2 u_v}{\partial y^2}\right) - \frac{\partial P}{\partial x} \tag{11}$$

Momentum in y-direction:

$$\rho_v \left(\frac{\partial v_v}{\partial t} + u_v \frac{\partial v_v}{\partial x} + v_v \frac{\partial v_v}{\partial y}\right) = \mu_v \left(\frac{\partial^2 v_v}{\partial x^2} + \frac{\partial^2 v_v}{\partial y^2}\right) - \frac{\partial P}{\partial y} \tag{12}$$

Energy:

$$\rho_v C_{p,v} \left(\frac{\partial T_v}{\partial t} + u_v \frac{\partial T_v}{\partial x} + v_v \frac{\partial T_v}{\partial y}\right) = k_v \left(\frac{\partial^2 T_v}{\partial x^2} + \frac{\partial^2 T_v}{\partial y^2}\right) + \dot{q} \tag{13}$$

Liquid Flow Region

$$\frac{\partial u_l}{\partial x} + \frac{\partial v_l}{\partial y} = 0 \tag{14}$$

The Darcy's Law is employed in the momentum equation for the porous liquid-wick region. The resulted unsteady momentum equation are:

Momentum in the x-direction:

$$\rho_l \left(\frac{\partial u_l}{\partial t} + u_v \frac{\partial u_l}{\partial x} + v_v \frac{\partial u_l}{\partial y}\right) = \mu_l \left(\frac{\partial^2 u_l}{\partial x^2} + \frac{\partial^2 u_l}{\partial y^2}\right) - \frac{\partial P}{\partial x} - \frac{\mu_l u_l \epsilon}{K} \tag{15}$$

Momentum in y-direction:

$$\rho_l \left(\frac{\partial v_l}{\partial t} + u_l \frac{\partial v_l}{\partial x} + v_l \frac{\partial v_l}{\partial y}\right) = \mu_l \left(\frac{\partial^2 v_l}{\partial x^2} + \frac{\partial^2 v_l}{\partial y^2}\right) - \frac{\partial P}{\partial y} - \frac{\mu_l u_l \epsilon}{K} \tag{16}$$

Energy:

$$\rho_l C_{p,l} \left(\frac{\partial T_l}{\partial t} + u_l \frac{\partial T_l}{\partial x} + v_l \frac{\partial T_l}{\partial y}\right) = k_{eff} \left(\frac{\partial^2 T_l}{\partial x^2} + \frac{\partial^2 T_l}{\partial y^2}\right) + \dot{q} \tag{17}$$

Boundary Conditions

The imposed boundary conditions are illustrated in Figure 3. The heat transfer coefficient, *h* can be determined using the Churchill and Chu correlation for the Nusselt number given below.

$$\overline{Nu}_d = \left\{0.60 + \frac{0.387 Ra_d^{1/6}}{\left[1 + (0.559/Pr)^{9/16}\right]^{8/27}}\right\}^2 \tag{18}$$

where Pr is the Prandtl number and Ra_d is the Rayleigh number.

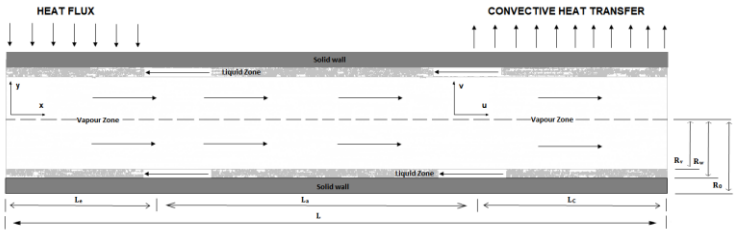

Figure 3 - Boundary conditions of heat pipe.

The detailed boundary conditions for evaporator, adiabatic and condenser region at the various radius and also at the ends of the heat pipe are given in Table 2 below.

Table 2 – Boundary Conditions

$N°$	Locations	Evaporator	Adiabatic	Condenser
1	Both ends of HP $(x = 0, L)$	$u = v = 0$ $\dot{m}_v = \frac{\dot{Q}}{h_{f,g}}$		$u = v = 0$
2	Centreline of HP $(y = 0)$	$v_v = 0,\ \frac{\partial v_v}{\partial y} = 0,\ \frac{\partial T_v}{\partial y} = 0$		
3	Liquid-vapour interface $(y = R_v)$	$\rho_v v_v = \rho_l v_l$		
4	Wick-wall interface $(y = R_w)$	$k_p \frac{\partial T_p}{\partial y} = k_{eff} \frac{\partial T_l}{\partial y}$, $u_l = v_l = 0,\ \rho_v v_v = \rho_l v_l = 0$		
5	Outer pipe wall $(y = R_0)$	$\dot{q} = k_p \frac{\partial T_p}{\partial y}$	$\frac{\partial T_p}{\partial y} = 0,\ \frac{\partial T_p}{\partial x} = 0$	$\frac{\partial T_p}{\partial y} = h(T_p - T_\infty)$

Method of Solution

The governing equations are discredited using a finite volume approach and equations were solved using SIMPLE algorithm. The unsteady state incompressible flow has been solved in both vapour and liquid region, using ANSYS Fluent software. The physical domain of problem was separated into 2 regions as follows.

1. vapour region;
2. liquid region and pipe wall

The numerical analysis was performed in both separated regions. The solution procedure is as follows.

1. Continuity and momentum equation are solved in vapour region with mentioned boundary conditions to find the pressure distribution;
2. Clausius-Clapeyron equation has been used to find temperature boundary condition at the liquid-vapour interface;
3. All of the equations have been solved in vapour region;
4. The mentioned equations with related boundary condition have been solved in liquid region and pipe wall simultaneously;

Discussion and Results

The temperature profiles to evaluate their thermal performance for wall power levels are shown by Figure 4a. Typically, the temperature of the outer wall of heat pipe's adiabatic section is selected as the parameter to study the response time since it shows the status of the heat pipe. First, to verify the operation functionality of the heat pipes the power step test was realized. This test was carried out with the heat pipes to evaluate the temperatures reached at each power applied at the moment of the start-up and of temperature stabilization, to obtain and initial analysis regarding their heat pipe transport capacity, and the behaviour of the evaporator in the change of each power. As the heat flux increases in the evaporator wall and the liquid (porous structure) that is in contact with the evaporator wall can progressively overheat and form bubbles at the nucleation sites. These bubbles can carry energy to the surface by latent heat of vaporization. With increasing heat flux, a critical value can be reached and dry-out of the porous structure that will potentially interrupt the operation of heat pipes.

For a better analysis of the heat transfer capacity of the heat pipes, the temperature difference between the evaporator and the condenser for each applied power was calculated (Figure 4b). A small

temperature difference between the evaporator and the condenser ensures proper operation and steady heat transfer by the heat pipes.

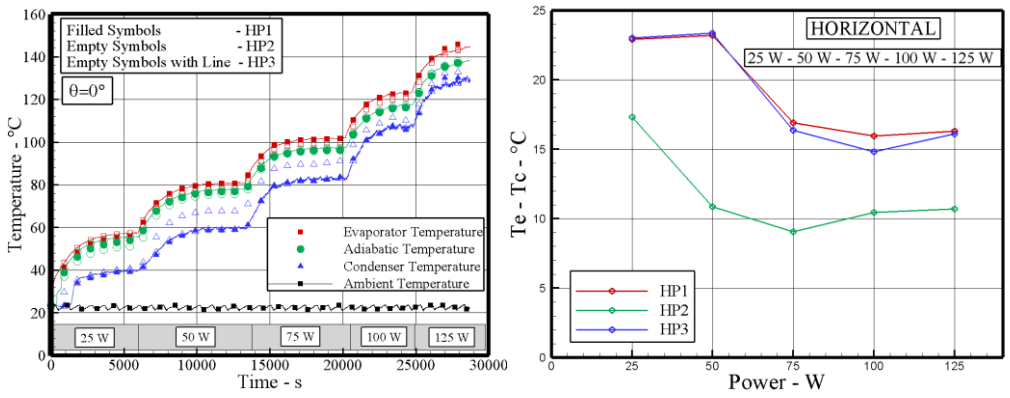

(a) (b)

Figure 4 – (a)Temperature profiles of HP1, HP2 and HP3 and (b) Temperature difference of heat pipes at different power.

The largest temperature difference between the evaporator and the condenser of approximately 23.35 ° C was presented for HP3 at 50 W and the lowest temperature difference was 6.75°C for the HP2 operating at 100W of applied power.

For the improved analysis, the experimantal thermal conductance of the heat pipe was calculated and compared with the calculated thermal conductance (Eq. 12), which considers an adjustment given by the variable factor that envolves uncontrolled variables that are innerhent to the manufacturing processes of the heat pipes and thermal conductance numerical. The calculated thermal conductance was introduced in the thermal resistence analysis (Eq. 6) along with the adjustment factor (Eq. 7) for each applied power, and the results of this comparison are presented by Figure 5.

The results show a good correlation between the experimental, calculated and numerical results. The proposed calculated thermal conductance and thermal conductance numerical, correctly predicted the increase in thermal conductance with the increase in the heat input and the same has been validated experimentally.

The highest experimental thermal conductance was obtained by HP2 of 12 W/°C and numerical thermal conductance the 12.7 W/°C. The heat pipe HP2 showed better thermal performance due to smaller pore size, lower porosity and permeability and higher capillary pressure. The theoretical thermal conductance presented results of approximately 9.6 W/°C for the HP1, 15.5 W/°C for the HP2 and 23 W/°C for the HP3.

Conclusions

The development of the heat pipe technology for industrial applications presents to be very important to improve the heat recovery systems performance, since they can greatly contribute to increase heat exchangers performances without great increase on their final costs. The continuous development of this technology for industrial purposes is highly desirable in order to give more degrees of freedom to thermal engineers to face the increase of heat dissipation and new challenges on thermal management issues.

For better thermal performance and conditions evaluation: the thermal profiles before and after the start-up, transient behavior during the changes on applying power, thermal behavior under steady state conditions were analyzed. The following conclusions were drawn from this study.

- The heat pipes presented stable behavior, for both transient and steady state conditions, when operated using the power levels of 25-125W. During the experimental tests, heat pipes did not present dry-out tendencies or superheat in the evaporator.
- The main objective of this study is a development of a numerical model that allows to perform simulation of the evaporation and condensation phenomena in heat pipes. The numerical model results of this paper show that FLUENT with the VOF method can successfully model the complex phenomena inside the heat pipe.

- The numerical thermal conductance has been verified with experimental thermal results and has shown good agreement.

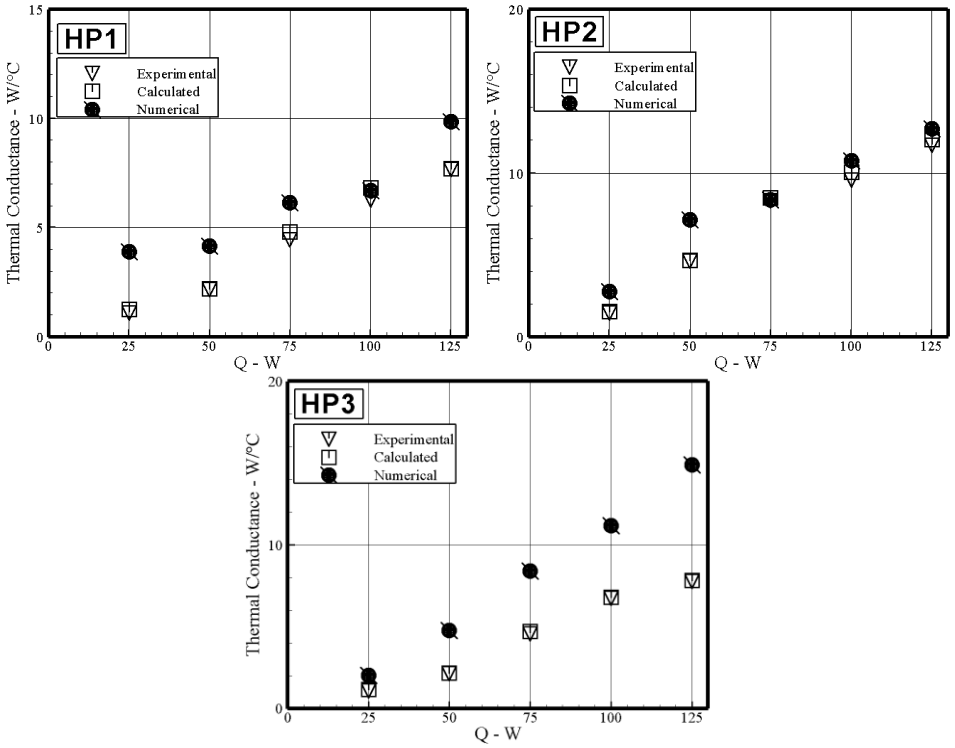

Figure 5 – Thermal conductance comparision between experimental, calculated and numerical for different heat inputs.

References:

[1] Riehl, R. R., Cachute, L., Thermal Control of Surveillance Systems Using Pulsating Heat Pipe and Heat Pipes, *Proceedings of the AIAA Propulsion and Energy Forum and Exposition 2013 - 11th Annual International Energy Conversion Engineering Conference (IECEC)*, July 15-17, San Jose, CA, 2013.

[2] Riehl, R. R., Passive thermal management of surveillance systems using pulsating heat pipes. *In: 9th Minsk International Seminar–Heat Pipes, Heat Pumps, Refrigerators, Power Sources*, 2015.

[3] Riehl, R. R. Utilization of passive thermal control technologies in cooling electronics: A brief review. *Heat Pipe Science and Technology: An International Journal*, Begell House Inc., v. 7, n. 3-4, pp. 161–183, 2016.

[4] Silva, D. de O., and Riehl R. R. Development of Heat Pipes Operating at Mid-Level Temperature Range Applied for Industry, Defense and Aerospace, *Proceedings of the AIAA Propulsion and Energy Forum 2014 - 12th International Energy Conversion Engineering Conference (IECEC)*, July 28-30, Cleveland, OH, 2014.

[5] J. M. Tournier, M. El-Genk, A transient analysis of water heat pipe, in: ASME Winter Conf., 28 Nov 1993, ASME, New Orleans, L.A, USA, 1993.

[6] Kempers, R., Ewing, D., and Ching, C. Y., Effect of number of mesh layers and fluid loading on the performance of screen mesh wicked heat pipes. *Applied Thermal Engineering*, 26(5), pp. 589-595, 2006.

[7] Kempers, R., Robinson, A. J., Ewing, D., and Ching, C. Y., Characterization of evaporator and condenser thermal resistances of a screen mesh wicked heat pipe. *International Journal of Heat and Mass Transfer*, 51(25), pp. 6039-6046, 2008.

[8] Silva, D. de O., Marcelino, E. W. and Riehl R. R. Thermal Performance Comparison Between Water-Copper and Water-Stainless Steel Heat Pipes. *13th International Energy Conversion Engineering Conference*, August 9-12, New York, USA, 2015.

[9] Silva, D. de O., Marcelino, E. W. and Riehl R. R., Experimental investigation of copper water heat pipes operation at mid-level temperature range for aerospace and industrial applications, *13th International Energy Conversion Engineering Conference*, August 9-12, New York, 2015.

[10] Chi, S.W., *Heat Pipe Theory and Practice*, Washington: Hemisphere Publishing Corporation, 1976.

[11] Reay, D. A., Kew, P. A., *Heat Pipes-theory, design and applications*, 5a Ed., Oxford, UK: Elsevier's Science & Technology, 2006.

CO selective methanation for PEMFC applications

P. Garbis, C. Kern and A. Jess

Chair of Chemical Engineering, University of Bayreuth, Universitätsstraße 40, 95440 Bayreuth
Center of Energy Technology (ZET), Universitätsstraße 30, 95447 Bayreuth

panagiota.garbis@uni-bayreuth.de

Abstract

The world's shift to alternative forms of energy production leads to the housing constructions which are independent from electricity prices and reduce CO_2 emission. In the recent years, the interest in the development of proton exchange membrane fuel cells (PEMFC) in stationary application is increased. PEMFCs could supply households with electrical power using natural gas or, as a perspective, biogas. As is well known, the compound CO is undesirable in the PEMFC operating gas, as CO degrades the PEMFC by poisoning the hydrogen oxidation reaction catalyst [1–3]. One of options to reduce the CO content to a value lower than 10 ppm is the selective methanation of CO [3–5]. For this purpose, supported noble metal catalysts were prepared by impregnation of γ-Al_2O_3 spheres and screened for the selective CO methanation. A manufactured Ru/Al_2O_3 catalyst was selected for further investigation. In this paper, the CO methanation with and without the presence of water is examined and a kinetic approach based on a Langmuir-Hinshelwood expression is suggested. Furthermore, the influence of CO_2 in the feed gas is presented.

Keywords: CO methanation, ruthenium, Fuel Cell, carbon monoxide, kinetic model

Introduction

PEMFCs have potential for generating electrical power in household use (see Fig. 1) by utilizing the hydrogen-containing gas produced from natural gas or, as a perspective, form biogas via steam reforming. Since the hydrogen production is always accompanied with such a by-product as carbon monoxide, which represents a strong poison for PEMFC, its content in the operating gas has to be reduced below the threshold values as to prevent the fuel cell catalyst degradation.

CO methanation can be considered an attractive technique to reduce the carbon monoxide content to guarantee the long life of PEMFCs. Conventionally, in the course of carbon monoxide methanation of a reformate gas, three main reactions can take place. viz.: CO methanation itself (Eq. (1)), CO_2 methanation (Eq. (2)) and the Reverse-Water-Gas-Shift (RWGS) reaction (Eq. (3)) where CO is produced again.

$$CO + 3\,H_2 \leftrightarrow CH_4 + H_2O \qquad \Delta H^0_{298} = -206\ \text{kJ mol}^{-1} \qquad (1)$$

$$CO_2 + 4\,H_2 \leftrightarrow CH_4 + 2\,H_2O \qquad \Delta H^0_{298} = -165\ \text{kJ mol}^{-1} \qquad (2)$$

$$CO_2 + H_2 \leftrightarrow CO + H_2O \qquad \Delta H^0_{298} = 41\ \text{kJ mol}^{-1} \qquad (3)$$

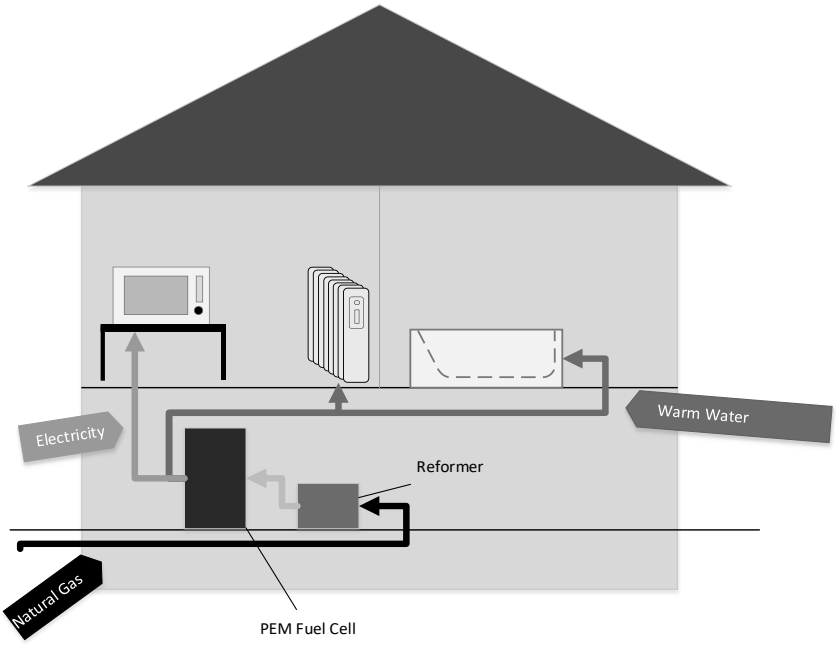

Figure 1: The idea of combined heat and power supply of households with natural gas.

For these purposes, different catalysts have been prepared to select the most appropriate one. The suitable catalyst should promote the CO methanation and at the same time suppress both the CO_2 methanation and the RWGS reaction. In the course of catalyst screening, a ruthenium based catalyst has indicated the highest activity and selectivity. A kinetic model for this catalyst including an inhibiting impact of water and carbon dioxide has been developed according to the Langmuir-Hinshelwood approach.

Discussion and Results

Experimental set-up and procedure

The experimental set-up (Fig. 2) consists of a fixed-bed reactor thermostated by an oil heating system. Two thermocouples in a guide tube are positioned in the catalyst bed to monitor the reaction temperature. The gas composition leaving the reactor is analysed with a gas analyser (X-STREAM Enhanced Process Gas Analyzer, Emerson) (CO, CO_2, H_2 and CH_4) and Gas Chromatography (long-chain hydrocarbons).

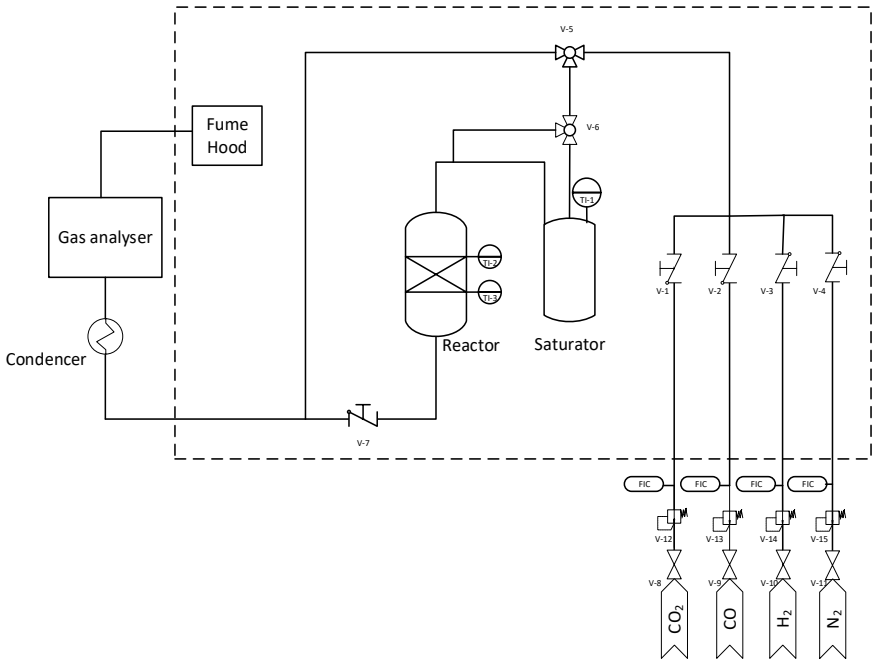

Figure 2: Experimental set-up.

The kinetics of CO methanation as well as the influence of H_2O on the reaction system is obtained for a Ru/Al_2O_3 catalyst. The reactor is charged with 2 g of catalyst particles diluted with 4 g of quartz sand, to keep the temperature of the catalyst bed stable. The reaction orders are defined in a temperature range from 160 to 185 °C by variation of the concentration of only one reactant (CO, H_2 or H_2O). N_2 is used in order to maintain the volumetric flow rate constant in each measurement. The volume flows are given at standard temperature and pressure conditions (STP) (T = 0°C, p = 1 bar).

Preparation and catalyst screening

Catalysts are prepared by wet impregnation of 2.5 mm Al_2O_3 spheres with ruthe-niumnitrosylnitrate $Ru(NO)(NO_3)_3$, cobalt (II) nitrate hexahydrate and manganese (II) nitrate. A commercial catalyst (2 wt% Ru supported on Al_2O_3) is also tested. After reduction by 10 vol% H_2 in N_2 at 350 °C, the catalysts are utilized in the methanation of CO. The catalyst loaded with 2 wt% Ru is further impregnated with NH_4Cl to improve selectivity of the CO methanation [2, 6].

Five catalysts are screened in order to find a suitable one for the selective CO methanation. Fig. 3 and Fig.4 show the conversion of CO and CO_2 over the examined catalysts. It is important to note that at temperatures over 230 °C, the RWGS reaction takes place producing CO which accounts for the negative CO conversion.

In comparison with the other catalysts, the Ru based catalysts indicate higher activity and selectivity. Although the catalyst loaded with 2 wt% Ru and 1.3 wt% Cl shows the highest selectivity, the catalyst is unsuitable for further applications. Since chloride is discharged from the catalyst bed during the run. Not only does not it guarantee the selectivity of the reaction, but could also affect the PEMFC. Therefore, the catalyst with 2 wt% Ru/Al_2O_3 is more preferable for further investigations.

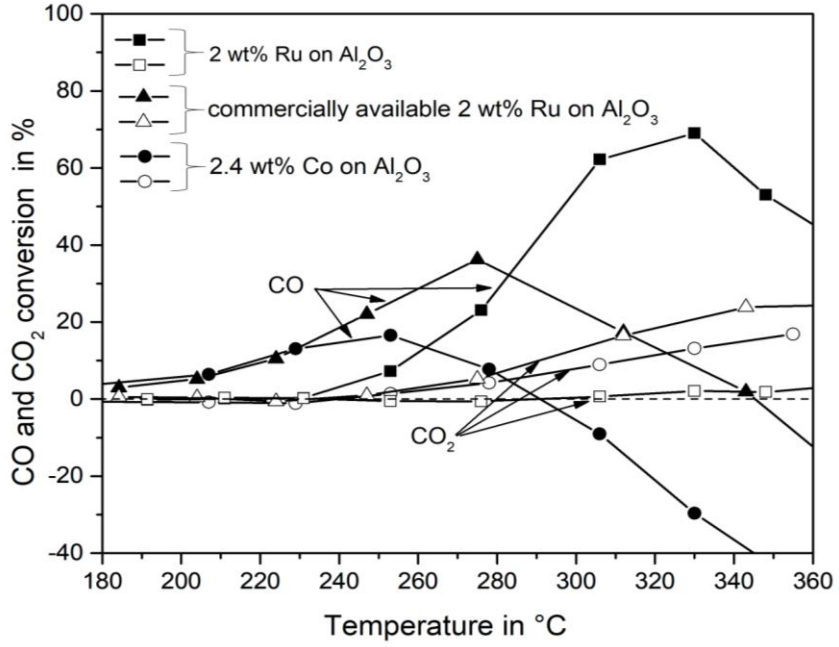

Figure 3: CO and CO_2 conversion as a function of reaction temperature; m_{cat} = 0.6 g; $\dot{V}_{STP}$= 68 l h^{-1} (1 vol% CO, 14 vol% CO_2, 30 vol% H_2, 55 vol% N_2).

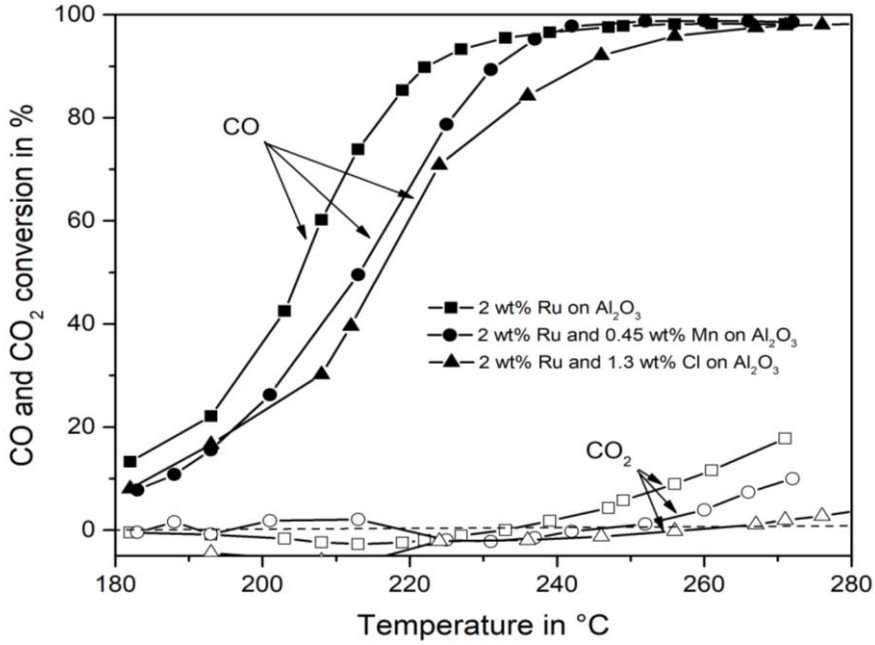

Figure 4: CO and CO_2 conversion as a function of reaction temperature; m_{cat} = 1.3 g; $\dot{V}_{STP}$= 10 l h^{-1}, (1 vol% CO, 10 vol% CO_2, 89 vol% H_2).

Kinetic of CO methanation

The reformate gas, which is the feed for the PEMFC, consist in particular of CO, H_2, H_2O and CO_2. For this reason, it is important to evaluate the impact of each component on CO methanation.

A kinetic approach based on a Langmuir-Hinshelwood approach (Eq. (4)) is suggested as

$$r_{CO} = -k(T)\frac{C_{CO}C_{H_2}}{\left(1 + K_1 C_{CO} + K_2 C_{H_2O}\right)^2}, \tag{4}$$

follows:

where C_i (i = CO, H_2, H_2O) is the gas concentration, K_1 and K_2 are the adsorption equilibrium constants for CO and H_2O, respectively and k(T) is the reaction rate constant according to the Arrhenius law (Eq. 5) :

$$k(T) = k_0 e^{\frac{-E_A}{RT}}, \tag{5}$$

here k_0 is the pre-exponential factor, E_A is the activation energy and R is the universal gas constant.

The reaction rate dependence on the CO concentration is shown in Fig. 5. As is seen, the CO and H_2O components demonstrate an inhibiting influence on the reaction rate. The defined parameters of the kinetic model are shown in Table 1.

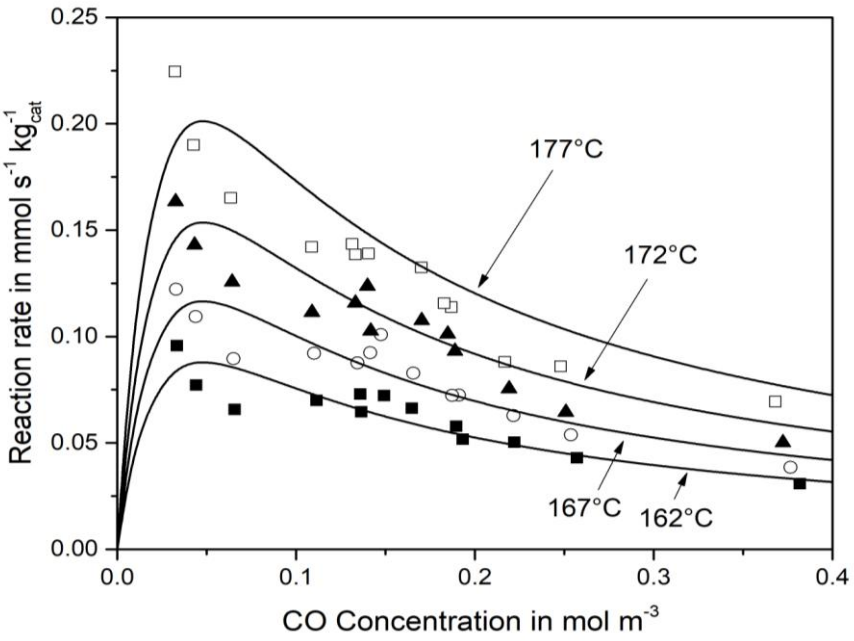

Figure 5: Reaction rate determined experimentally compared with calculated from Eq.(4) in the range from 162°C to 177°C. 0.4 - 1.4 vol% CO, 55 vol% H_2, Rest N_2, m_{cat} = 2g; $\dot{V}_{STP}$= 15 l h^{-1}.

Table 1: Parameters of the kinetic model

Parameter	
pre-exponential factor, k_0	3.61 10^7 m^6 s^{-1} kg^{-1} mol^{-1}
Activation energy, E_A	90.000 J mol^{-1}
adsorption equilibrium constant for CO, K_1	23 m^3 mol^{-1}
adsorption equilibrium constant for H_2O, K_2	0.3 m^3 mol^{-1}

Through integration of Eq. 4, the CO conversion was calculated and compared to the experimental data (Fig. 6). As is seen, the kinetic model of the CO methanation very well corresponds to the experimental data.

Since CO_2 has to be a content of the feed gas, the influence of CO_2 in the CO methanation was examined. It turned out that CO_2 had a small inhibiting effect on the CO conversion (Fig. 7) which could be neglected. Furthermore, no CO_2 conversion was noticed for temperatures lower than 220 °C.

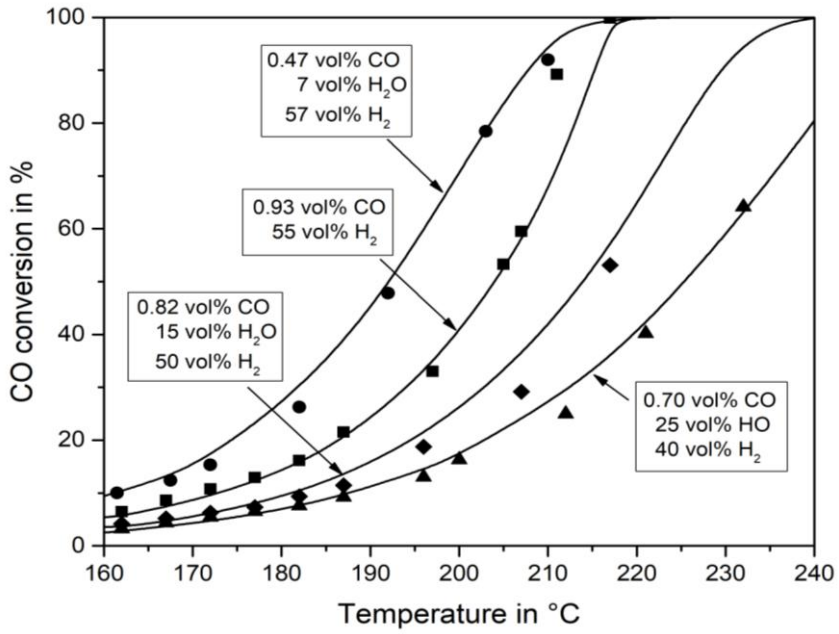

Figure 6: Comparison of experimental with modelled CO conversion for different inlet gas compositions in the feed gas. m_{cat} = 2g; $\dot{V}_{STP}$ = 17 l h^{-1}.

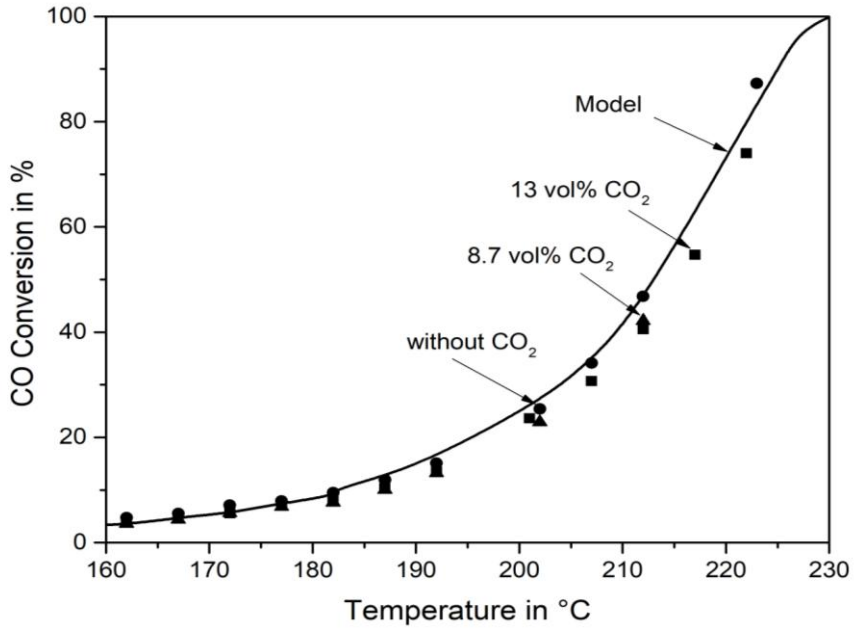

Figure 7: Impact of CO_2 on CO conversion. 1.15 vol% CO, 55 vol% H_2, rest balanced with N_2; m_{cat} = 2g; $\dot{V}_{STP}$ = 15 l h^{-1}.

The next aim is the expansion of the kinetic model in order to describe the selective CO methanation. For this purpose, further experiments have to take place by a varying of the CO_2 concentrations.

Conclusions

After catalyst screening, the synthesized catalyst loaded with 2 wt% Ru on Al_2O_3 represented the highest activity and selectivity for the selective CO methanation. A kinetic model, based on a Langmuir-Hinshelwood approach, was suggested for the CO methanation taking into consideration H_2O in the feed gas. The influence of CO_2 in the CO methanation was investigated. CO_2 has an almost negligible inhibiting effect on the methanation of CO. Our first results are promising for the further efforts in developing a catalyst and model for the selective CO methanation.

Acknowledgements

This work has been funded by the Bavarian State Ministry of Education, Science and the Arts within the framework "TechnologieAllianzOberfranken (TAO)". The authors gratefully acknowledge this support.

References

[1] Baschuk, J. J. and Li, X., Carbon monoxide poisoning of proton exchange membrane fuel cells, Int. J. Energy Res., 2001, DOI:10.1002/er.713.

[2] Djinovi, P., Galletti, C., Specchia, S., and Specchia, V., CO Methanation Over Ru, Top Catal, 2011, DOI:10.1007/s11244-011-9724-8.

[3] Djinović, P., Galletti, C., Specchia, S., and Specchia, V., Ru-based catalysts for CO selective methanation reaction in H2-rich gases, Catalysis Today, 2011, DOI:10.1016/j.cattod.2010.11.007.
[4] Eckle, S., Denkwitz, Y., and Behm, R. J., Activity, selectivity, and adsorbed reaction intermediates/reaction side products in the selective methanation of CO in reformate gases on supported Ru catalysts, Journal of Catalysis, 2010, DOI:10.1016/j.jcat.2009.10.025.
[5] Jiménez, V., Sánchez, P., Panagiotopoulou, P., Valverde, J. L., and Romero, A., Methanation of CO, CO2 and selective methanation of CO, in mixtures of CO and CO2, over ruthenium carbon nanofibers catalysts, Applied Catalysis A: General, 2010, DOI:10.1016/j.apcata.2010.09.026.
[6] Miyao, T., Shen, W., Chen, A., Higashiyama, K., and Watanabe, M., Mechanistic study of the effect of chlorine on selective CO methanation over Ni alumina-based catalysts, Applied Catalysis A: General, 2014, DOI:10.1016/j.apcata.2014.08.025.